ADVANCED SCIENCE Open Access
www.advancedscience.com

Constructing Localized Van Der Waals Gaps in Cubic-Phase $GeMnTe_2$ Thermoelectric Material

Mingrui Zhang, Lingling Wei, Tingting Yang, Weishuai Wang, Fudong Zhang, Mengqi Li, Beiquan Jia, Yalin Shi, Zupei Yang, Rafal E. Dunin-Borkowski, Lei Jin,* and Di Wu**

Cubic-phase $GeMnTe_2$ shows high potential to replace state-of-the-art rhombohedral GeTe for medium temperature thermoelectric application owing to its lower cost. The high structural symmetry can also suppress phase transition during service and provides a superior platform for further band and microstructural engineering. Through Sb_2Te_3 alloying and Pb substitution, this study realizes a superior peak figure of merit of ≈1.5 at 773 K and a remarkable average figure of merit of ≈0.96 at 323–823 K. Sb_2Te_3 alloying successfully generates high-density localized van der Waals (vdW) gaps which are able to scattering low-frequency phonons effectively for reduced lattice conductivity; meanwhile, it also enlarges the valence band degeneracy for enhanced power factor. Pb substitution further reduces the hole concentration to an optimal level. The achievements in this work well reveal the efficacy of construing localized vdW gaps in improving matrix material's thermoelectric performance, thus might shed light on other cubic or pseudo-cubic thermoelectric systems.

1. Introduction

Thermoelectric materials are a unique class of functional materials that can directly convert heat into electricity (Seebeck effect) or vice versa (Peltier effect).[1–3] Due to their potential applications in power generation and solid-state refrigeration,[4–7] thermoelectric materials attracted considerable attentions in recent decades. The performance of a thermoelectric material is primarily evaluated by the dimensionless figure of merit ZT, defined as $ZT = (S^2\sigma T)/\kappa_{tot}$, where S is the Seebeck coefficient, σ is electrical conductivity, T is the absolute temperature in Kelvin, and κ_{tot} is total thermal conductivity (comprising electronic part κ_{ele} and lattice part κ_{lat}). Naturally, a high ZT value requires a large power factor ($PF = S^2\sigma$) and simultaneously a low κ_{tot};[8–10] unfortunately, the interdependence of base parameters (S, σ, and κ_{tot}) makes ZT enhancement quite challenging. Till now, strategies that have been used to enhance peak ZT can fall into one or the combination of the following points, including but not limited to modulating electronic bands, charge transfer engineering, optimizing carrier concentration, introducing point defects and/or nanostructure/dislocations, refining grains.[11–22]

In addition to pursuing higher peak ZT, it is also of practical importance to achieve high average thermoelectric performance (i.e., average ZT) in a wider temperature range (in most cases at medium or high temperatures). Since the phase of a thermoelectric material during service is usually not its naturally stable form at low or room temperature, stabilization of this high-performance (and high-temperature) phase to low or even room temperature becomes a possible approach, as reported for SnSe,[23–25] $Cu_{2-x}S$,[26] GeTe, *etc.* As for GeTe-based materials with room temperature (RT) rhombohedral structure (space group: $R3m$), the ZT value can easily exceed 2.5 via band engineering and microstructure complication.[27–29] However, a phase transition from rhombohedral to cubic structure at ≈700 K,[30] is detrimental to achieving high average ZT as well as to maintaining good thermodynamic stability of thermoelectric module in the scenario of medium temperature service.[31,32] In contrast, recent studies show that reaction of rhombohedral GeTe and hexagonal MnTe can create a pseudo-binary compound of $GeMnTe_2$ (or written as $Ge_{0.5}Mn_{0.5}Te$), which exhibits a rock salt cubic structure at RT (space group: $Fm\bar{3}m$) and p-type conducting behavior.[33,34] The high-symmetry crystal structure of $GeMnTe_2$ as compared with rhombohedral GeTe results in a highly degenerated valence band structure, which is constructive to assure

M. Zhang, W. Wang, F. Zhang, M. Li, B. Jia, Y. Shi, Z. Yang, D. Wu
Key Laboratory for Macromolecular Science of Shaanxi Province and Shaanxi Key Laboratory for Advanced Energy Devices
School of Materials Science and Engineering
Shaanxi Normal University
Xi'an 710119, China
E-mail: wud@snnu.edu.cn

L. Wei
School of Chemistry and Chemical Engineering
Shaanxi Normal University
Xi'an 710119, China
E-mail: weill@snnu.edu.cn

T. Yang, R. E. Dunin-Borkowski, L. Jin
Ernst Ruska-Centre for Microscopy and Spectroscopy with Electrons
Forschungszentrum Jülich GmbH
52425 Jülich, Germany
E-mail: l.jin@fz-juelich.de

The ORCID identification number(s) for the author(s) of this article can be found under https://doi.org/10.1002/advs.202517830

DOI: 10.1002/advs.202517830

high ZT;[35–37] Meanwhile, it eliminates the unwanted phase transition up to the working temperatures and also provides a superior platform for further microstructural engineering. In addition, the disordered distribution of Ge and Mn at cationic sites leads to intense phonon scattering rate thus quite low lattice thermal conductivity.[33,36,38] Furthermore, because of the less consumption of Ge in $GeMnTe_2$, it shows a superior price advantage over the GeTe-base materials. However, the extremely high intrinsic hole concentration ($\approx 10^{21}$ cm^{-3}) resulting from the large number of cation vacancies becomes the major obstruction of realizing decent thermoelectric performance in $GeMnTe_2$.

In recent years, constructing localized van der Waals (vdW) planar defect structure in high-symmetry lattice exhibits great potential in improving thermoelectric performance of matrix materials. Here, localized vdW is used in order to distinguish those that are intrinsically present (thus laterally wide and often periodically stacked) in layered vdW materials. It has been reported that Sb_2Te_3 alloying can successfully trigger localized vdW gaps in rhombohedral GeTe and cubic SnTe lattice.[39–41] With nanoscale lateral dimensions and atomic-scale vertical gaps, localized vdW gaps scatter phonons significantly and scatter carriers weakly compared to the laterally wide gaps,[39,42,43] thus realizing the so-call discriminately scattering of charge carriers and heat-carrying phonons. It should be noted that higher symmetry (e.g., cubic) usually represents higher density of localized vdW gaps that can be introduced to the structure, which provides an extra parameter for microstructure engineering.

In this work, we first regulate the molar ratio of Ge/Mn in $Ge_{1-x}Mn_xTe$ matrix in order to optimize the basal composition, then alloy Sb_2Te_3 into the basal material to construct localized vdW gaps like in GeTe;[44–46] afterward, we optimize the hole concentration by doping Pb at Mn site. Ultimately, we achieve a notably improved thermoelectric performance in the composition of $(Ge_{0.45}Mn_{0.4}Pb_{0.15}Te)_{0.8}(Sb_{2/3}Te)_{0.2}$. The maximal ZT value reaches ≈1.5 at 773 K, and the average ZT value is ≈0.96 at the temperature range of 323–823 K. Meanwhile, the Vickers hardness H_v is obviously enhanced from 180.7 for pristine $GeMnTe_2$ to 230.7 for $(Ge_{0.45}Mn_{0.4}Pb_{0.15}Te)_{0.8}(Sb_{2/3}Te)_{0.2}$. This work reveals that $GeMnTe_2$ could stand as a robust medium temperature thermoelectric material and that constructing localized vdW gaps could diversify the optimizing strategy for higher thermoelectric performance.

2. Results and Discussion

Figure 1a shows the replotted pseudo-binary phase diagram of GeTe-MnTe.[34] It can be seen that $Ge_{1-x}Mn_xTe$ can retain cubic structure when x lies between 0.18 to 0.55 and becomes a coexistence of cubic and hexagonal structures thereafter ($x >$ 0.55). In literature, the composition of $Ge_{0.5}Mn_{0.5}Te$ ($x = 0.5$) with a stable cubic structure at RT was used for thermoelectric studies.[36,38,47] In this work, we first adjust the molar ratio of Ge/Mn in $Ge_{1-x}Mn_xTe$ to optimize the basal material while maintaining the cubic structure. For the sake of cost, we increase x starting from $x = 0.5$. Figure 1b depicts the powder X-ray diffraction (XRD) patterns of obtained $Ge_{1-x}Mn_xTe$ ($x = 0.5$, 0.55, 0.6, 0.7, and 0.8) samples, and details of sample synthesis can be found in the Supporting Information (SI). All samples exhibit the cubic phase structure, and the measured lattice parameter decreases gradually as Mn content x increases, as shown in Figure 1c. This is mainly due to the smaller ionic radius of Mn^{2+} (0.67Å) as compared to Ge^{2+} (0.73 Å). Besides the dominant cubic phase, Ge precipitates are observed for $x = 0.5$, 0.55, and 0.6, and when x exceeds 0.7, diffraction peaks of $MnTe_2$ appears. When x increases further to 0.8, a large number of heterogeneous Mn-rich precipitations are observed in Figure 1d using scanning electron microscopy (SEM) and associated energy dispersive X-ray spectroscopy (EDS), in consistence with XRD results.

The thermoelectric performance of $Ge_{1-x}Mn_xTe$ ($x = 0.5$, 0.55, 0.6, 0.7, and 0.8) is shown in **Figure 2**. The electrical conductivity σ initially decreases and subsequently increases with elevating temperature, as shown in Figure 2a, which might be related to the thermal excitation of minority charge carriers. Moreover, σ tends to decrease with increasing Mn content x, which is opposite to the behavior of Seebeck coefficient S as shown in Figure 2b. The S values of all these samples are positive, exhibiting a p-type character with hole as the dominant charge carriers. Specifically, S at RT can rise significantly up to 163 μV K^{-1} in the sample with $x = 0.7$, as compared to only 84 μV K^{-1} for the control sample $Ge_{0.5}Mn_{0.5}Te$. The total thermal conductivity κ_{tot} is reduced from 2.2 W m^{-1} K^{-1} for $Ge_{0.5}Mn_{0.5}Te$ to 1.8 W m^{-1} K^{-1} for $Ge_{0.45}Mn_{0.55}Te$ at RT, and the upturn of κ_{tot} at high temperature is attributed to the bipolar effects (Figure 2c).[48,49] Eventually, the $Ge_{0.45}Mn_{0.55}Te$ sample exhibits a comparable maximal ZT of ≈0.8 at 773 K with the control sample $Ge_{0.5}Mn_{0.5}Te$, but a much higher average ZT of ≈0.5 from 323 to 773 K (Figure 2d).

Now the optimized $Ge_{0.45}Mn_{0.55}Te$ is used as a matrix material, and further modulation is realized by alloying different amounts of Sb_2Te_3 to the matrix. The synthesized samples with molar ratio y of Sb_2Te_3 are written as $(Ge_{0.45}Mn_{0.55}Te)_{1-y}(Sb_{2/3}Te)_y$ ($y = 0.05$, 0.1, 0.15, 0.20, and 0.25), and their phase structure and lattice constants are shown in Figure S1a,b (Supporting Information). All samples exhibit a single cubic phase structure until a secondary Sb_2Te_3 phase emerges when $y = 0.25$. **Figure 3a–f** shows the thermoelectric properties of $(Ge_{0.45}Mn_{0.55}Te)_{1-y}(Sb_{2/3}Te)_y$ (y = 0.05, 0.1, 0.15, 0.2, and 0.25) samples. With the increase of y, σ gradually decreases from 826 to 330 S cm^{-1} at RT; meanwhile, S increases significantly. Despite a slight reduction in PF, its value still remains at a relatively high level. Upon Sb_2Te_3 alloying, the κ_{tot} value at 323 K decreases from 1.8 W m^{-1} K^{-1} for $Ge_{0.45}Mn_{0.55}Te$ matrix to 1.13 W m^{-1} K^{-1} for the sample with y = 0.2 (Figure 3d). The calculated lattice thermal conductivity κ_{lat} is shown in Figure 3e. It is obvious that alloying Sb_2Te_3 results in a significant and systematic reduction in κ_{lat}. It is also noted that the κ_{lat} after Sb_2Te_3 alloying exhibits anomaly at ≈500–600 K. Since there is no detectable secondary phase in XRD, we performed SEM and EDS analysis on the $y = 0.05$ sample (Figure S1c,d, Supporting Information) and observed trace amounts of Ge/Mn-rich precipitations with size of 5–10 μm. We infer that the anomaly of electrical conductivity and electronic thermal conductivity probably results from the dissolution of the Ge/Mn-rich secondary phase into the matrix at approximately 550 K. Due to the significant reduction in κ_{tot} and the high level of PF, the $(Ge_{0.45}Mn_{0.55}Te)_{0.8}(Sb_{2/3}Te)_{0.2}$ sample exhibits a peak ZT value of 0.96 at 773 K, which is 20% higher than that of pristine $Ge_{0.45}Mn_{0.55}Te$ matrix.

To illuminate the underlying reason for increased ZT upon Sb_2Te_3 alloying, we performed first-principles density functional

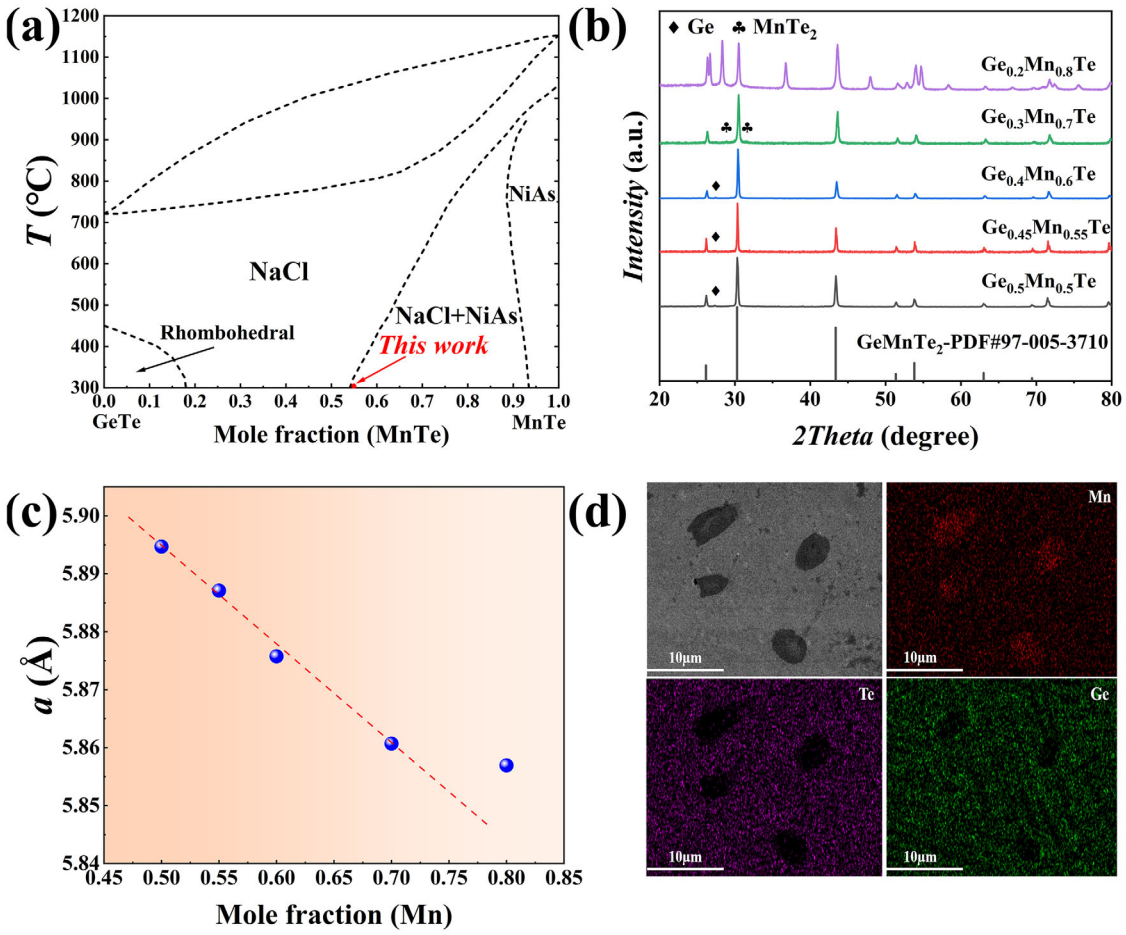

Figure 1. a) Replotted GeTe-MnTe pseudo-binary phase diagram based on Ref.;[34] b) powder XRD patterns of $Ge_{1-x}Mn_xTe$ (x = 0.5, 0.55, 0.6, 0.7, and 0.8), c) measured lattice parameters (of dominant cubic phase) as a function of Mn content x; d) SEM and corresponding EDS results of the $Ge_{0.2}Mn_{0.8}Te$ sample.

theory (DFT) calculations by VASP (Vienna Ab initio Simulation Package) to evaluate the band structure changes.[50,51] Details can be found in SI. A special quasi-random structure (details in Figure S2, Supporting Information) was constructed to serve as the supercell for DFT calculations.[52] For simplification and without loss of generality, Figure 3g,h shows the obtained electronic band structures of $Ge_{12}Mn_{12}Te_{24}$ (= $Ge_{0.5}Mn_{0.5}Te$) and $Ge_{10}Mn_{10}Sb_4Te_{24}$ (= $Ge_{0.42}Mn_{0.42}Sb_{0.17}Te$, which is close to $(Ge_{0.45}Mn_{0.55}Te)_{0.8}(Sb_{2/3}Te)_{0.2}$≈ $Ge_{0.36}Mn_{0.44}Sb_{0.13}Te$), respectively. Significant changes in the band structure can be found upon Sb_2Te_3 alloying. In addition to the reduction of band gap, more valence band peaks emerge at K point to Γ and L points (VB_2, VB_5, VB_6) and the energy difference among these peaks is extremely small, leading to significant enlargement of band degeneracy N_v (projected density of states and partial density of states near Fermi level are shown in Figure S3, Supporting Information). The changes of band structure give rise to remarkable increase in S, which compensates the reduction of σ, thus, the PF value can be maintained at the high level as shown in Figure 3c.

Like GeTe, the extremely low cation vacancy formation energy in $Ge_{0.5}Mn_{0.5}Te$ leads to a very high hole concentration (≈10^{21} cm^{-3}).[47] Such a high intrinsic carrier concentration typically stands against the advance of its thermoelectric performance. To increase the cation vacancy formation energy for a reduced hole concentration, we use Pb as the substitution element at Mn sites. Through DFT calculations, we find that the cation vacancy formation energies $E(V_{Ge})$ of the Pb-free sample ($Ge_{12}Mn_{12}Te_{24}$) and Pb-incorporated sample (e.g., $Ge_{10}Mn_{10}Pb_4Te_{24}$) are 0.548 and 4.098 eV, respectively. The significant increase of cation vacancy formation energy is expected to result in obvious hole concentration reduction, which is evidenced by our Hall measurements (**Figure 4**). Figure S4 (Supporting Information) shows the XRD patterns and lattice constants obtained from $(Ge_{0.45}Mn_{0.55-z}Pb_zTe)_{0.8}(Sb_{2/3}Te)_{0.2}$ (z = 0, 0.05, 0.1, 0.15, and 0.175) samples.

The measured thermoelectric properties are shown in Figure 4. With the increase of z, σ decreases gradually (Figure 4a) while S behaves in the opposite direction (Figure 4b). Specifically, at 323 K, σ drops from 331 S cm^{-1} for z = 0 to 87 S cm^{-1} for z = 0.175. Correspondingly, S rises from 131 to 254 μV K^{-1}. Hall measurements at RT (Figure 4c) reveal a significant and systematic reduction in hole concentration alongside a notable improvement in carrier mobility. Furthermore, the weighted mobility μ_w, an important parameter that can quantify the charge carrier

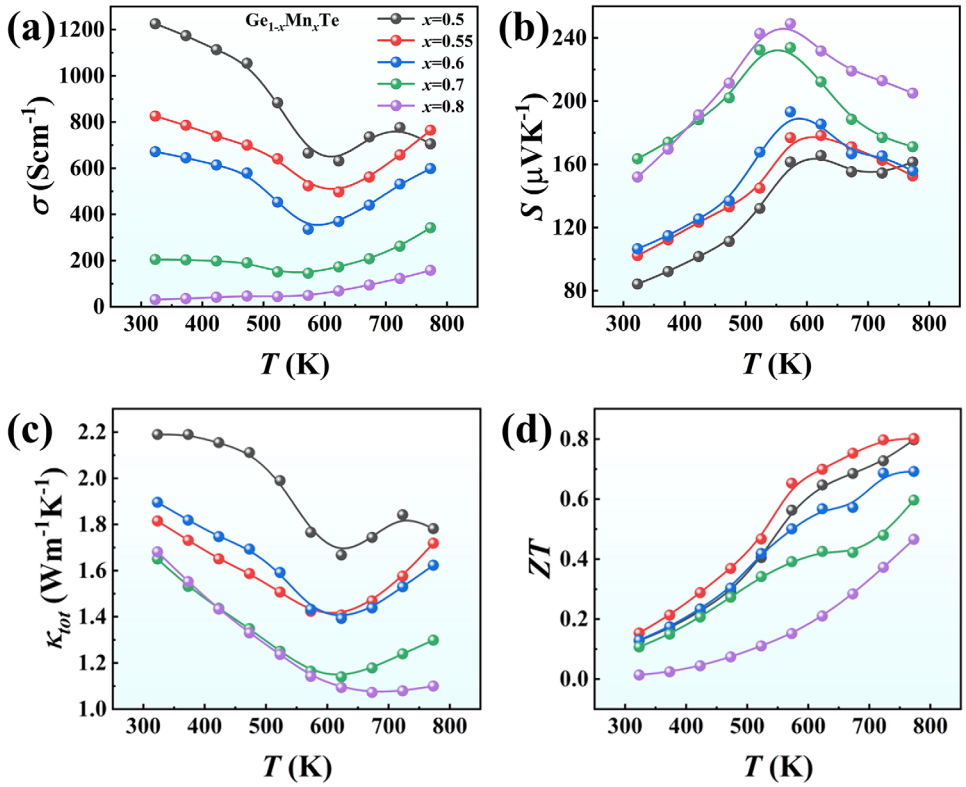

Figure 2. Temperature dependence of a) electrical conductivity σ, b) Seebeck coefficient S, c) thermal conductivity κ_{tot}, and d) figure of merit ZT for $Ge_{1-x}Mn_xTe$ ($x = 0.5$, 0.55, 0.6, 0.7, and 0.8).

transport efficiency, is calculated and presented in Figure 4d.[53] It can be seen that the RT μ_w reaches a maximum of ≈83 cm^2 V^{-1} s^{-1} as Pb content $z = 0.1$, suggesting a significant weakening of charge carrier scattering. Due to the large increase in S, the PF values of Pb-incorporated samples are slightly enhanced, *i.e.*, a maximum PF of 18 μW cm^{-1} K^{-2} is realized at 823 K in the composition of $(Ge_{0.45}Mn_{0.4}Pb_{0.15}Te)_{0.8}(Sb_{2/3}Te)_{0.2}$ (Figure 4e). The κ_{tot} is reduced significantly over the entire temperature range from 323 to 823 K; especially, the RT value reduces from 1.13 W m^{-1} K^{-1} for $(Ge_{0.45}Mn_{0.55}Te)_{0.8}(Sb_{2/3}Te)_{0.2}$ to 0.73 W m^{-1} K^{-1} for $(Ge_{0.45}Mn_{0.4}Pb_{0.15}Te)_{0.8}(Sb_{2/3}Te)_{0.2}$, as shown in Figure 4f. Figure 4g represents the calculated κ_{lat} as a function of T for different z values; the lowest κ_{tot} reaches ≈0.4 W m^{-1} K^{-1} at 773 K for the sample with $z = 0.15$, which is close to the amorphous limit.[54–56] The synergistic optimization of the electrical and thermal transport properties push figure of merit ZT to a maximum of 1.5 at 773 K in the composition of $(Ge_{0.45}Mn_{0.4}Pb_{0.15}Te)_{0.8}(Sb_{2/3}Te)_{0.2}$, which is ≈80% higher than that of the Pb-free ones (Figure 4h).

The microstructure of $(Ge_{0.45}Mn_{0.4}Pb_{0.15}Te)_{0.8}(Sb_{2/3}Te)_{0.2}$ is investigated using (scanning) transmission electron microscopy ((S)TEM), as shown in **Figure 5**. First, the cubic structure of $(Ge_{0.45}Mn_{0.4}Pb_{0.15}Te)_{0.8}(Sb_{2/3}Te)_{0.2}$ matrix grains is confirmed by systematic tilting series of selected area electron diffraction (Figure S5, Supporting Information). At grain boundaries, PbTe and Mn/Ge-rich precipitates are evident, as shown in Figure S6 (Supporting Information), their size is about 50–100 nm. Besides, high-magnification high-angle annular dark-field (HAADF) STEM images as shown in Figure 5b and Figure S7 (Supporting Information) display the formation of high density localized vdW gaps inside the matrix grains. These vdW gaps are in the {111} habit planes which are close-packed and result in the diffused streak contrast in the corresponding fast Fourier transfer (FFT) image (indicated by arrows in the inset of Figure 5b). Digital dark-field image using the selected streak areas (see dashed ellipses) highlights the localized vdW gaps, as shown in Figure S8a (Supporting Information) and the strain components calculated by using geometric phase analysis,[57] as shown in Figure S8b–d, reveal that the lattice distortion is confined in the vicinity of localized vdW gaps. In comparison, no such localized microstructure as well as streak contrast is evidenced in the pristine $Ge_{0.45}Mn_{0.55}Te$ as shown in Figure 5a. Finally, atomic-resolution HAADF STEM images shown in Figure 5c,d reveal the close-up configuration of localized vdW gaps in the $(Ge_{0.45}Mn_{0.4}Pb_{0.15}Te)_{0.8}(Sb_{2/3}Te)_{0.2}$ (≈ $Ge_{0.36}Mn_{0.32}Pb_{0.12}Sb_{0.13}Te$) sample. The bright dots in the grain matrix represent heavier Te atoms while the dark represent (in average) lighter cation atoms dominated by of Ge and Mn. This is further confirmed by image simulation and atomic resolution EDS, as shown in Figure 5e. It should be noted that the atomic number of Sb is next to Te, while its nominal concentration is about 1/10 of the latter. This leads to severe challenge in spatially resolving Sb using spectroscopy against Te. For further analysis, we perform layer-by-layer average for the marked regions (white parallelograms) to improve signal-to-noise ratio and the resulting images are shown as insets outlined by white rectangles together

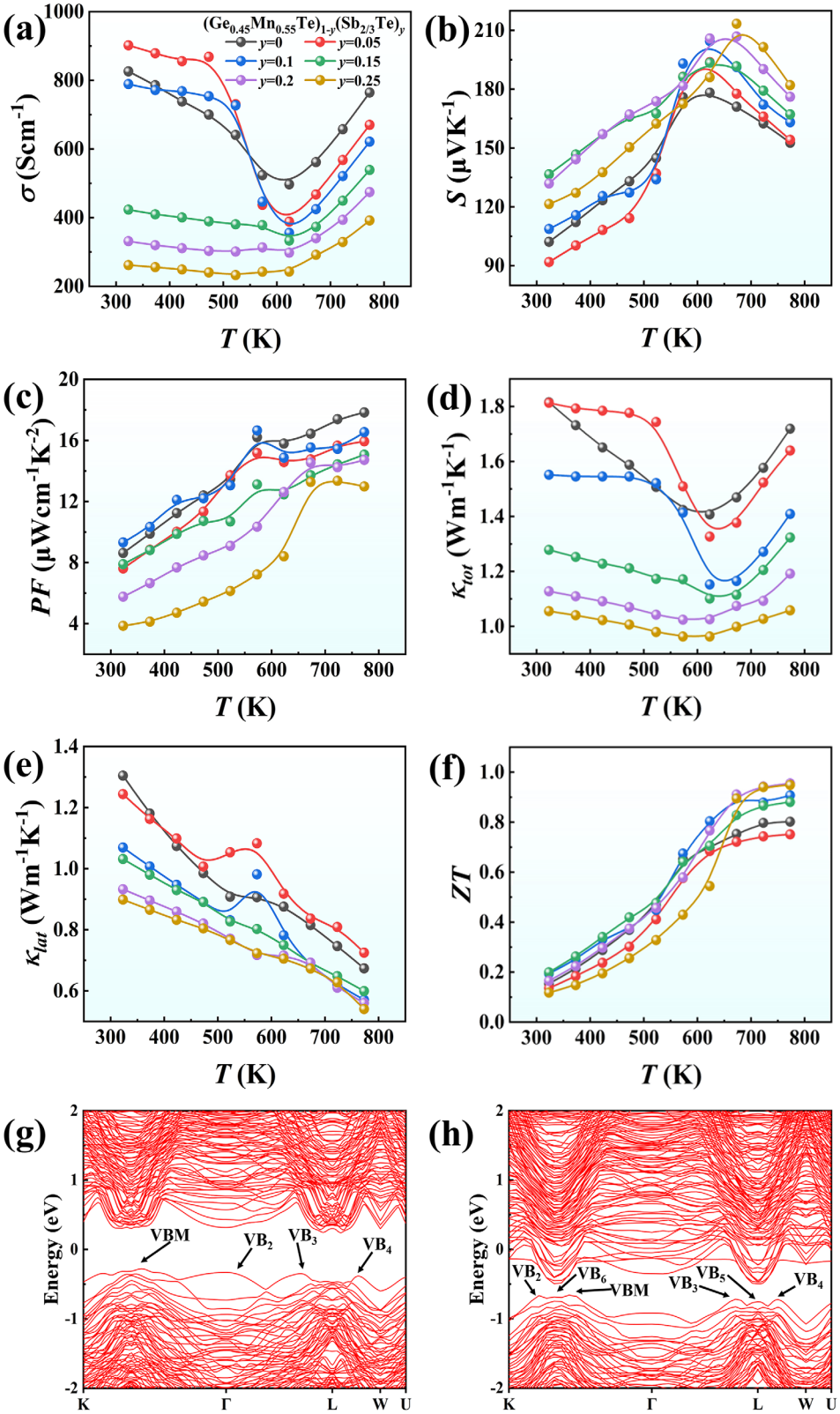

Figure 3. Temperature dependence of a) electrical conductivity σ, b) Seebeck coefficient S, c) power factor PF, d) thermal conductivity κ_{tot}, e) lattice thermal conductivity κ_{lat}, and f) figure of merit ZT for $(Ge_{0.45}Mn_{0.55}Te)_{1-y}(Sb_{2/3}Te)_y$ (y = 0, 0.05, 0.1, 0.15, 0.2, and 0.25). Calculated electronic band structures of e) $Ge_{12}Mn_{12}Te_{24}$ and (f) $Ge_{10}Mn_{10}Sb_4Te_{24}$.

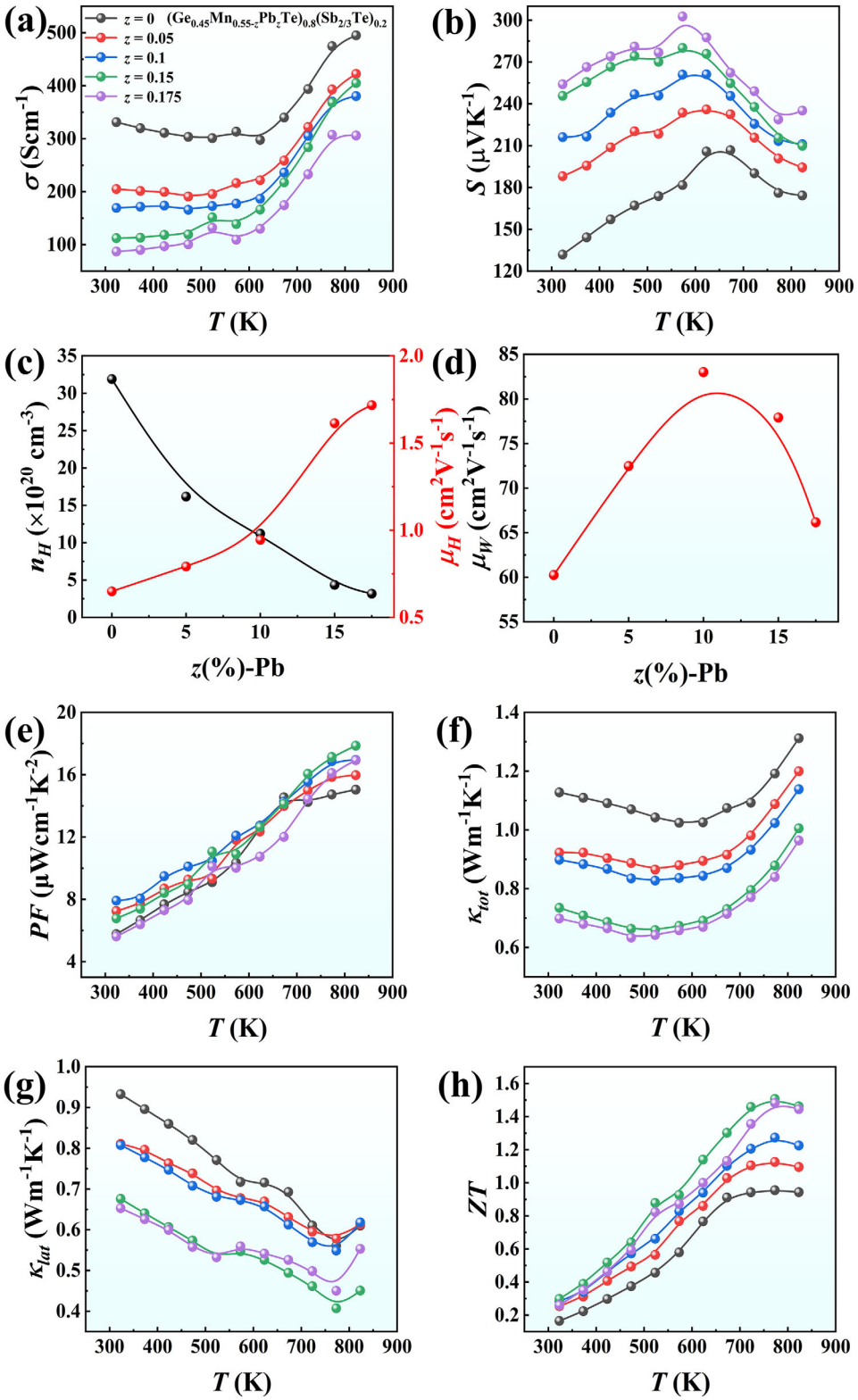

Figure 4. Temperature dependent a) electrical conductivity σ and b) Seebeck coefficient S. c) Room-temperature carrier concentration n_H and mobility μ_H, and d) calculated weighted mobility μ_w as a function of Pb content z. Temperature dependent e) power factor PF, f) total thermal conductivity κ_{tot}, g) lattice thermal conductivity κ_{lat}, and h) figure of merit ZT for $(Ge_{0.45}Mn_{0.55-z}Pb_zTe)_{0.8}(Sb_{2/3}Te)_{0.2}$ (z = 0, 0.05, 0.1, 0.15, and 0.175) samples.

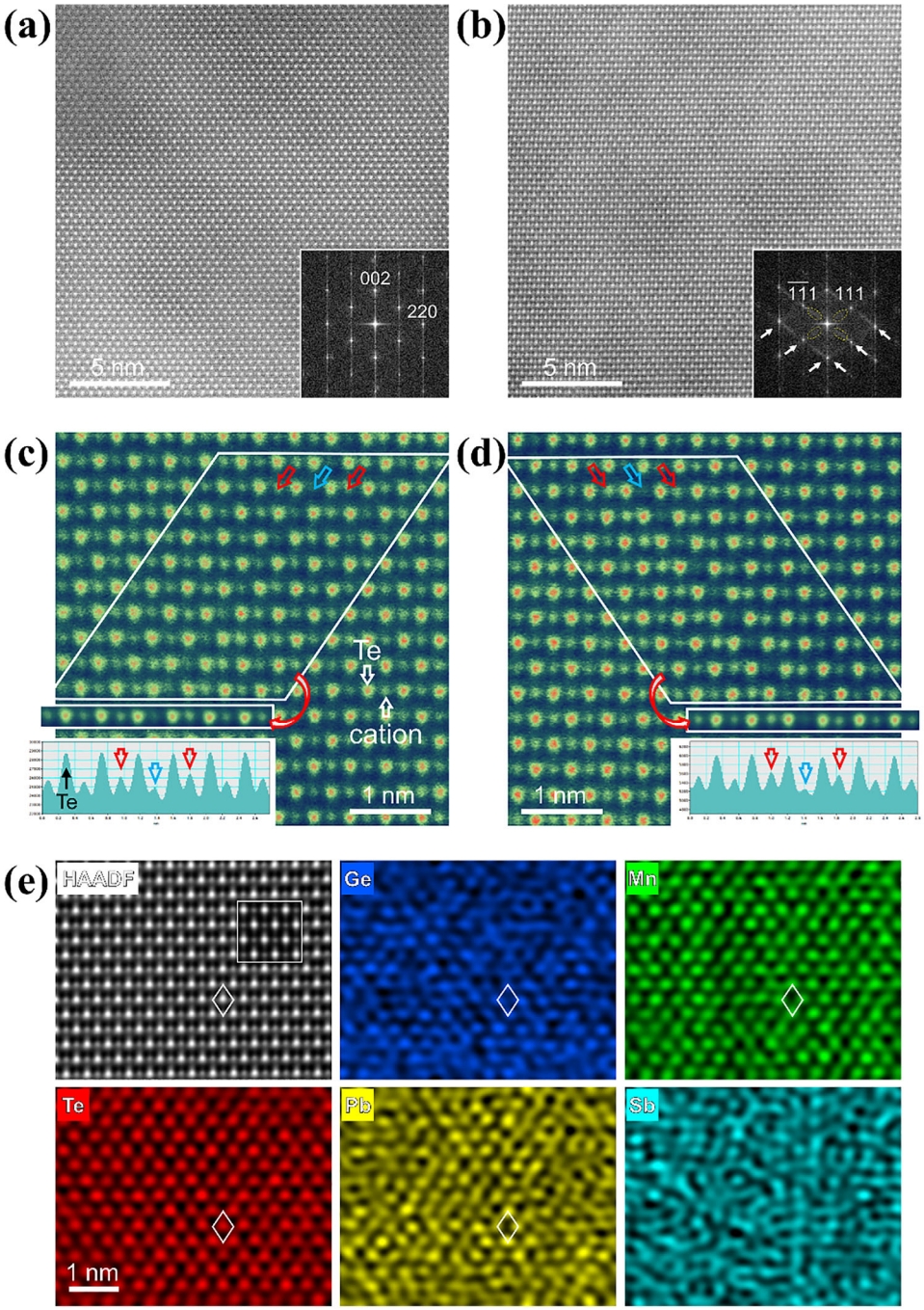

Figure 5. HAADF STEM image and corresponding FFT image (inset) of a) $Ge_{0.45}Mn_{0.55}Te$ and b) $(Ge_{0.45}Mn_{0.4}Pb_{0.15}Te)_{0.8}(Sb_{2/3}Te)_{0.2}$. The diffused streak contrast resulting from the presence of localized vdW gaps are indicated by arrows in (b). c,d) Atomic-resolution HAADF images and the intensity line profiles of the layer-by-layer averaged images (outlined by rectangles) obtained from the marked area (by parallelograms). e) Atomic-resolution HAADF image and corresponding EDS mapping from the $(Ge_{0.45}Mn_{0.4}Pb_{0.15}Te)_{0.8}(Sb_{2/3}Te)_{0.2}$ matrix. The cation positions are indicated by rhombus. Inset: simulated image.

with the intensity line profiles of atomic columns. It should be also noted that the lateral width of localized vdW gaps is in the range of 10 nm (e.g., see vdW gap 2 in Figure S7, Supporting Information), while the thickness of our TEM sample is about 50–100 nm. This inevitably leads to a situation that the gap overlaps with the grain matrix, thus residual (but low) atomic intensities are still visible, as indicated by blue arrows, which are most likely from the matrix atoms.

The loss of cations in the localized vdW gaps is expected to cause charge imbalance, as we don't see clear intensity changes at the Te columns. To neutralize the local charges, more cations are accumulated to the adjacent columns, as indicated by red

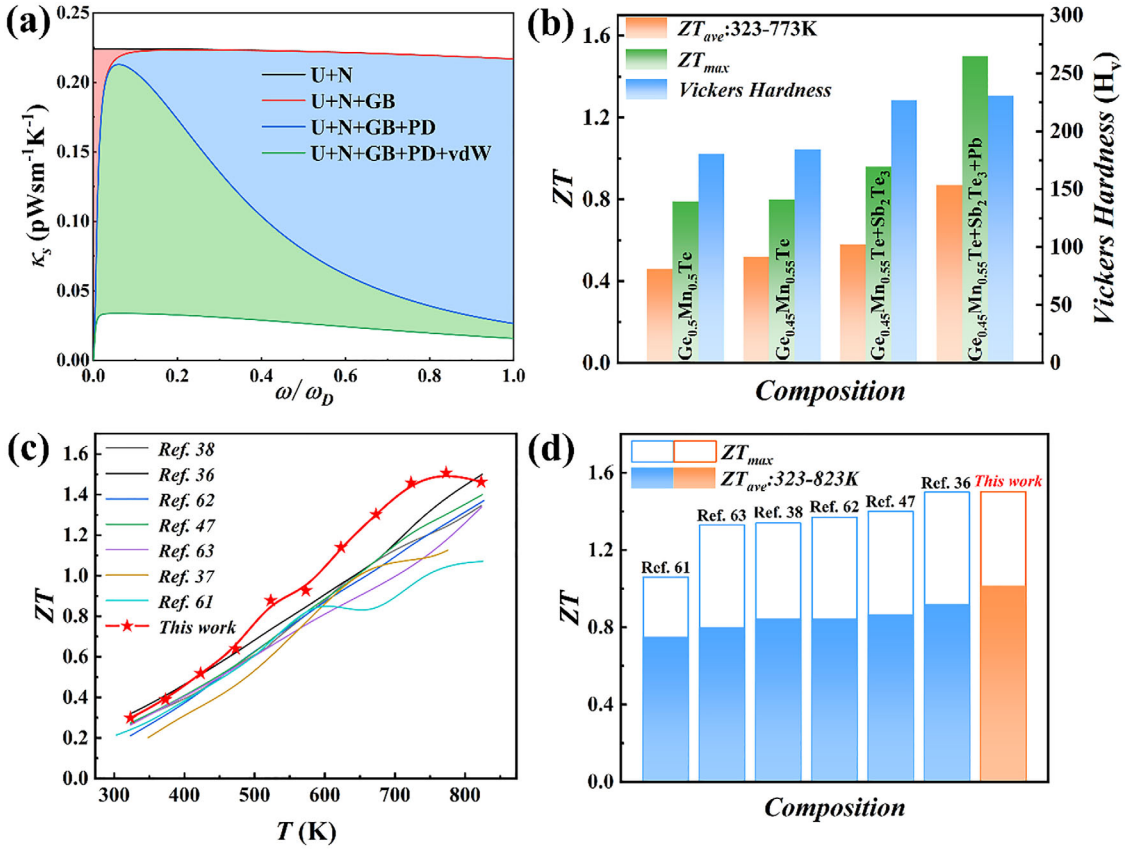

Figure 6. a) Calculated RT spectral lattice thermal conductivity (κ_s) as a function of phonon frequency based on Debye–Callaway model. b) Stepwise enhancements of ZT_{max}, ZT_{ave}, and H_v in this work. Comparison of c) temperature-dependent ZT and d) ZT_{max} and ZT_{ave} achieved in this work with $GeMnTe_2$-based materials in literatures, where the corresponding compositions are $Ge_{0.8}Na_{0.1}Bi_{0.1}MnTe_2$,[61] $(Sb_2Te_3)_{0.5}(Ge_{0.91}Pb_{0.09}Te)_{17.5}$,[37] $Ge_{0.7}Mn(AgBi)_{0.15}Te_2$-3%Sb,[63] $Ge_{0.9}MnSb_{0.1}Te_2$,[38] $Ge_{0.94}Bi_{0.06}MnTe_{1.94}Se_{0.06}$,[62] $Ge_{0.92}Pb_{0.08}MnTe_2$,[47] $GeMnTe_2$-15.1%SbTe.[36]

arrows. This provides a different mechanism from the case of GeTe,[58,59] in which the formation of vdW gaps are correlated with the presence of charged head-to-head domains. More gaps and corresponding line profiles can be found in Figure S7 (Supporting Information).

To figure out how microstructures affect the phonon transport, we calculate the temperature dependent κ_{lat} as well as the RT spectral lattice thermal conductivity (κ_s) based on Debye–Callaway model (details in SI) by considering different scattering mechanisms including Umklapp processes (U), normal processes (N), grain boundaries (GB), point defects (PD) and localized vdW gaps. It is seen that our simulated temperature dependent κ_{lat} agrees quite well with experimental ones (Figure S9, Supporting Information). Moreover, as seen in **Figure 6**a, the reduction of lattice thermal conductivity at high-frequency region originates mainly from point defects scattering, considering the fact that evenly distributed Pb/Sb atoms provide strong mass and strain fluctuation as revealed by the aforementioned microstructure characterizations. Meanwhile, abundant localized vdW gaps as revealed in Figure 5 and Figure S7 (Supporting Information) are able to significantly weaken the low-frequency phonon transport.

So far, we have realized stepwise enhancements of thermoelectric performance based on the cubic-phase $Ge_{0.5}Mn_{0.5}Te$. Specifically, the peak ZT (ZT_{max}) increases from 0.8 for $Ge_{0.5}Mn_{0.5}Te$ to 1.5 for $(Ge_{0.45}Mn_{0.4}Pb_{0.15}Te)_{0.8}(Sb_{2/3}Te)_{0.2}$, and the average ZT (ZT_{ave}) from 0.46 to 0.87 in the temperature range of 323–773 K. We also achieve a significant enhancement of Vicker's hardness H_v (see Figure S10, Supporting Information, for details), i.e., H_v reaches 230.7 in $(Ge_{0.45}Mn_{0.4}Pb_{0.15}Te)_{0.8}(Sb_{2/3}Te)_{0.2}$, which is 25% higher than the control sample $Ge_{0.5}Mn_{0.5}Te$ and 72% higher than pristine rhombohedral GeTe.[60] The results are summarized in Figure 6b. In Figure 6c,d, we compare the achievement in this work with state-of-the-art $Ge_{0.5}Mn_{0.5}Te$-based thermoelectric materials in literatures,[36–38,47,61–63] the $(Ge_{0.45}Mn_{0.4}Pb_{0.15}Te)_{0.8}(Sb_{2/3}Te)_{0.2}$ sample exhibits an outstandingly high ZT_{max} of ≈1.5 at 773 K and remarkably large ZT_{ave} of ≈0.96 between 323 and 823 K.

3. Conclusion

In this work, we successfully construct high-density localized vdW gaps via Sb_2Te_3 alloying with the optimized cubic phase $Ge_{0.45}Mn_{0.55}Te$. The localized vdW gaps poses strong scattering on low-frequency phonons and effectively reduces the κ_{lat}. Moreover, Sb_2Te_3 alloying enlarges the valence band convergence in favor of high PF. We also optimize the carrier concentration and improve the weighted mobility by Pb substitution at cation

sites, which results in strong phonon scattering in the high-frequency region. Eventually an ultralow κ_{lat} down to 0.4 W m^{-1} K^{-1} is achieved at 773 K in $(Ge_{0.45}Mn_{0.4}Pb_{0.15}Te)_{0.8}(Sb_{2/3}Te)_{0.2}$. This leads to an outstanding peak ZT of ≈1.5 at 773 K and a remarkable average ZT of ≈0.96 at 323–823 K in the composition of $(Ge_{0.45}Mn_{0.4}Pb_{0.15}Te)_{0.8}(Sb_{2/3}Te)_{0.2}$, exceeding almost all $Ge_{0.5}Mn_{0.5}Te$-based thermoelectric materials reported so far.

4. Experimental Section

The experimental details can be found in the Supporting Information.

Supporting Information

Supporting Information is available from the Wiley Online Library or from the author.

Acknowledgements

This work was supported by the National Natural Science Foundation of China (Grant Nos. 52272119), the Fundamental Research Funds for the Central Universities (Program No. GK202401009), the Natural Science Basic Research Plan in the Shaanxi Province of China (Grant No. 2024JC–YBMS–385), and the Fundamental Innovation Project in the School of Materials Science and Engineering. The authors also thank the support of the Shaanxi Sanqin Scholars Innovation Team.

Open access funding enabled and organized by Projekt DEAL.

Conflict of Interest

The authors declare no conflict of interest.

Data Availability Statement

The data that support the findings of this study are available from the corresponding author upon reasonable request.

Keywords

cubic $GeMnTe_2$, synergistic optimization, thermoelectric materials, van der Waals gap

Received: September 11, 2025
Revised: October 23, 2025
Published online: November 3, 2025

[1] L. E. Bell, *Science* **2008**, *321*, 1457.
[2] J. Mao, G. Chen, Z. Ren, *Nat. Mater.* **2021**, *20*, 454.
[3] W. Liu, Q. Jie, H. S. Kim, Z. Ren, *Acta Mater.* **2015**, *87*, 357.
[4] J. Zhu, X. Tan, M. Hong, Y. Wei, H. Ma, F. Feng, Y. Luo, H. Wu, Q. Sun, R. Ang, *Adv. Energy Mater.* **2024**, *14*, 2402552.
[5] X. Hao, J. Wang, H. Wang, *Chem. Soc. Rev.* **2025**, *54*, 1957.
[6] D. Beretta, N. Neophytou, J. M. Hodges, M. G. Kanatzidis, D. Narducci, M. Martin-Gonzalez, M. Beekman, B. Balke, G. Cerretti, W. Tremel, A. Zevalkink, A. I. Hofmann, C. Müller, B. Dörling, M. Campoy-Quiles, M. Caironi, *Mater. Sci. Eng.: R: Reports* **2019**, *138*, 100501.
[7] T. Xing, Q. Song, P. Qiu, Q. Zhang, M. Gu, X. Xia, J. Liao, X. Shi, L. Chen, *Energy Environ. Sci.* **2021**, *14*, 995.
[8] J. He, I. D. Blum, H.-Q. Wang, S. N. Girard, J. Doak, L.-D. Zhao, J.-C. Zheng, G. Casillas, C. Wolverton, M. Jose-Yacaman, D. N. Seidman, M. G. Kanatzidis, V. P. Dravid, *Nano Lett.* **2012**, *12*, 5979.
[9] Q. Yang, S. Yang, P. Qiu, L. Peng, T.-R. Wei, Z. Zheng, X. Shi, L. Chen, *Science* **2022**, *377*, 854.
[10] Y. Luo, J. Yang, Q. Jiang, W. Li, D. Zhang, Z. Zhou, Y. Cheng, Y. Ren, X. He, *Adv. Energy Mater.* **2016**, *6*, 1600007.
[11] Y. Pei, H. Wang, G. J. Snyder, *Adv. Mater.* **2012**, *24*, 6125.
[12] L.-D. Zhao, G. Tan, S. Hao, J. He, Y. Pei, H. Chi, H. Wang, S. Gong, H. Xu, V. P. Dravid, C. Uher, G. J. Snyder, C. Wolverton, M. G. Kanatzidis, *Science* **2016**, *351*, 141.
[13] J. Mao, J. L. Niedziela, Y. Wang, Y. Xia, B. Ge, Z. Liu, J. Zhou, Z. Ren, W. Liu, M. K. Y. Chan, G. Chen, O. Delaire, Q. Zhang, Z. Ren, *Nano Energy* **2018**, *48*, 189.
[14] Q. Zhang, P. Ying, A. Farrukh, Y. Gong, J. Liu, X. Huang, D. Li, M. Wang, G. Chen, G. Tang, *Acta Mater.* **2024**, *276*, 120132.
[15] D. Wu, X. Chen, F. Zheng, H. Du, L. Jin, R. E. Dunin-Borkowski, *ACS Appl. Energy Mater.* **2019**, *2*, 2392.
[16] A. Li, L. Wang, J. Li, T. Mori, *Energy Environ. Sci.* **2024**, *17*, 8810.
[17] W. Li, S. Lin, B. Ge, J. Yang, W. Zhang, Y. Pei, *Adv. Sci.* **2016**, *3*, 1600196.
[18] X. Zhang, J. Li, X. Wang, Z. Chen, J. Mao, Y. Chen, Y. Pei, *J. Am. Chem. Soc.* **2018**, *140*, 15883.
[19] A. J. Minnich, M. S. Dresselhaus, Z. F. Ren, G. Chen, *Energy Environ. Sci.* **2009**, *2*, 466.
[20] F. Mao, Z. Zhang, S. Zhu, C. Liu, J. Gao, J.-L. Chen, X. Wang, T. Xing, L. Miao, *J. Materiomics.* **2025**, https://doi.org/10.1016/j.jmat.2025.101108.
[21] K. Chen, Q. Sun, H. Li, X. Tan, J. Cai, Z. Guo, Z. Zhang, G. Liu, J. Wu, J. Jiang, *Small* **2025**, *21*, 2502510.
[22] C. Liu, Z. Zhang, Y. Peng, F. Li, L. Miao, E. Nishibori, R. Chetty, X. Bai, R. Si, J. Gao, X. Wang, Y. Zhu, N. Wang, H. Wei, T. Mori, *Sci. Adv.* **2023**, *9*, eadh0713.
[23] B. E. Matthews, A. M. Holder, L. T. Schelhas, S. Siol, J. W. May, M. R. Forkner, D. Vigil-Fowler, M. F. Toney, J. D. Perkins, B. P. Gorman, A. Zakutayev, S. Lany, J. Tate, *J. Mater. Chem. A* **2017**, *5*, 16873.
[24] S.-K. Cha, S. Im, Y.-S. Kim, *ACS Appl. Energy Mater.* **2022**, *5*, 2067.
[25] S.-K. Cha, S. Im, B. Ryu, Y.-S. Kim, *Current Appl. Phys.* **2023**, *45*, 45.
[26] T.-Y. Yang, S.-W. Gu, Y.-X. Zhang, F. Zheng, D. Kong, R. E. Dunin-Borkowski, D. Wu, Z.-H. Ge, J. Feng, L. Jin, *Adv. Mater.* **2024**, *36*, 2308353.
[27] T. Xing, C. Zhu, Q. Song, H. Huang, J. Xiao, D. Ren, M. Shi, P. Qiu, X. Shi, F. Xu, L. Chen, *Adv. Mater.* **2021**, *33*, 2008773.
[28] T. Zhang, S. Deng, X. Zhao, X. Ruan, N. Qi, Z. Chen, X. Su, X. Tang, *J. Mater. Chem. A* **2022**, *10*, 3698.
[29] D. Sarkar, M. Samanta, T. Ghosh, K. Dolui, S. Das, K. Saurabh, D. Sanyal, K. Biswas, *Energy Environ. Sci.* **2022**, *15*, 4625.
[30] T. Chatterji, C. M. N. Kumar, U. D. Wdowik, *Phys. Rev. B* **2015**, *91*, 054110.
[31] W.-D. Liu, D.-Z. Wang, Q. Liu, W. Zhou, Z. Shao, Z.-G. Chen, *Adv. Energy Mater.* **2020**, *10*, 2000367.
[32] Q. Sun, K. Chen, X. Tan, H. Li, G. Wu, Z. Guo, J. Cai, G.-Q. Liu, J. Wu, J. Jiang, *Small* **2025**, *21*, 2500333.
[33] B. Zhou, W. Li, X. Wang, J. Li, L. Zheng, B. Gao, X. Zhang, Y. Pei, *Sci. China Mater.* **2019**, *62*, 379.
[34] W. D. Johnston, D. E. Sestrich, *J. Inorg. Nucl. Chem.* **1961**, *19*, 229.
[35] Q. Mei, C. Xie, J. Liu, Y. Wang, J. Cui, L. Liao, C. Liao, W. Xu, S. Li, Q. Zhang, X. Tang, G. Tan, *Adv. Energy Mater.* **2025**, *15*, 2500937.
[36] J. Dong, Y. Jiang, Y. Sun, J. Liu, J. Pei, W. Li, X. Y. Tan, L. Hu, N. Jia, B. Xu, Q. Li, J.-F. Li, Q. Yan, M. G. Kanatzidis, *J. Am. Chem. Soc.* **2023**, *145*, 1988.
[37] L. Gao, W. Li, S. Wei, X. Yang, Z. Ji, W. Song, S. Zheng, *Status Solidi B* **2023**, *260*, 2200507.

[38] Q. Mei, C. Xie, J. Cui, C. Liao, S. Li, X. Tang, G. Tan, *Acta Mater.* **2025**, *285*, 120694.
[39] X. Xu, L. Xie, Q. Lou, D. Wu, J. He, *Adv. Sci.* **2018**, *5*, 1801514.
[40] T. Rosenthal, M. N. Schneider, C. Stiewe, M. Döblinger, O. Oeckler, *Chem. Mater.* **2011**, *23*, 4349.
[41] X. Xu, J. Cui, Y. Yu, B. Zhu, Y. Huang, L. Xie, D. Wu, J. He, *Energy Environ. Sci.* **2020**, *13*, 5135.
[42] X. Qi, Y. Yu, X. Xu, J. Wang, F. Zhang, B. Zhu, J. He, X. Chao, Z. Yang, D. Wu, *Mater. Today Phys.* **2021**, *21*, 100507.
[43] J. Wang, Y. Yu, J. He, J. Wang, B. Ma, X. Chao, Z. Yang, D. Wu, *ACS Appl. Energy Mater.* **2021**, *4*, 14608.
[44] X. Xu, Y. Huang, L. Xie, D. Wu, Z. Ge, J. He, *Chem. Mater.* **2020**, *32*, 1693.
[45] Y. Chen, H. Wu, G. Han, B. Zhang, X. Lu, W. Yang, G. Wang, X. Han, X. Zhou, *Materiomics* **2025**, *11*, 100973.
[46] S. Chen, K. Liu, T. Luo, L. Liao, Z. Yang, S. Zhong, J. Wu, X. Su, P. F. P. Poudeu, Q. Zhang, X. Tang, *Mater. Today Phys.* **2024**, *45*, 101455.
[47] J. Dong, J. Pei, H.-L. Zhuang, H. Hu, B. Cai, J.-F. Li, *J. Mater. Chem. A* **2019**, *7*, 27361.
[48] N. Li, W. He, C. Li, G. Wang, G. Wang, X. Zhou, X. Lu, *J. Mater. Chem. A* **2021**, *9*, 2385.
[49] X. Wang, H. Yao, L. Yin, W. Xue, Z. Zhang, S. Duan, L. Chen, C. Chen, J. Sui, X. Liu, Y. Wang, J. Mao, Q. Zhang, X. Lin, *Adv. Energy Mater.* **2022**, *12*, 2201043.
[50] J. P. Perdew, K. Burke, M. Ernzerhof, *Phys. Rev. Lett.* **1996**, *77*, 3865.
[51] G. Kresse, J. Furthmüller, *Phys. Rev. B* **1996**, *54*, 11169.
[52] S. H. Wei, L. G. Ferreira, J. E. Bernard, A. Zunger, *Phys. Rev. B* **1990**, *42*, 9622.
[53] G. J. Snyder, A. H. Snyder, M. Wood, R. Gurunathan, B. H. Snyder, C. Niu, *Adv. Mater.* **2020**, *32*, 2001537.
[54] D. G. Cahill, S. K. Watson, R. O. Pohl, *Phys. Rev. B* **1992**, *46*, 6131.
[55] M. T. Agne, R. Hanus, G. J. Snyder, *Energy Environ. Sci.* **2018**, *11*, 609.
[56] T. Ghosh, M. Dutta, D. Sarkar, K. Biswas, *J. Am. Chem. Soc.* **2022**, *144*, 10099.
[57] M. J. Hÿtch, E. Snoeck, R. Kilaas, *Ultramicroscopy* **1998**, *74*, 131.
[58] Y. Yu, L. Xie, S. J. Pennycook, M. Bosman, J. He, *Sci. Adv.* **2022**, *8*, add7690.
[59] Y. Yu, X. Xu, Y. Wang, B. Jia, S. Huang, X. Qiang, B. Zhu, P. Lin, B. Jiang, S. Liu, X. Qi, K. Pan, D. Wu, H. Lu, M. Bosman, S. J. Pennycook, L. Xie, J. He, *Nat. Commun.* **2022**, *13*, 5612.
[60] S. Zhi, J. Li, L. Hu, J. Li, N. Li, H. Wu, F. Liu, C. Zhang, W. Ao, H. Xie, X. Zhao, S. J. Pennycook, T. Zhu, *Adv. Sci.* **2021**, *8*, 2100220.
[61] Y. Zhang, L. Xu, G.-Q. Liu, J. Cai, Y. Yin, F. Shi, X. Tan, J. Jiang, *Phys. Chem. Chem. Phys.* **2021**, *23*, 17866.
[62] S. Duan, Y. Yin, G.-Q. Liu, N. Man, J. Cai, X. Tan, K. Guo, X. Yang, J. Jiang, *Research* **2021**, *2021*, 1949070.
[63] Y. Zhong, S. Chen, J. Cai, Z. Zhang, F. Gao, S. Huo, J. Wu, C. Cui, X. Tan, G. Liu, J. Jiang, *Electron. Mater.* **2024**, *6*, 2552.

Supporting Information

Constructing Localized van der Waals Gaps in Cubic-phase $GeMnTe_2$ Thermoelectric Material

Mingrui Zhang, Lingling Wei, Tingting Yang, Weishuai Wang, Fudong Zhang, Mengqi Li, Beiquan Jia, Yalin Shi, Zupei Yang, Rafal E. Dunin-Borkowski, Lei Jin*, and Di Wu**

Experimental Section

1. Sample Synthesis

All samples were prepared by high-temperature melting combined with spark plasma sintering (SPS) technology. For the samples of composition $Ge_{1-x}Mn_xTe$ (x = 0.5, 0.55, 0.6, 0.7 and 0.8), $(Ge_{0.45}Mn_{0.55}Te)_{1-y}(Sb_{2/3}Te)_y$ (y = 0.05, 0.1, 0.15, 0.2 and 0.25), $(Ge_{0.45}Mn_{0.55-z}Pb_zTe)_{0.8}(Sb_{2/3}Te)_{0.2}$ (z = 0.05, 0.1, 0.15 and 0.175), high purity Ge (99.99%, Aex), Mn (99.99%, Aladdin), Sb (99.99%, Aladdin), Te (99.99%, Aex), Pb (99.99%, Aladdin) particles were weighted according to stoichiometric ratio and sealed in quartz tube under a vacuum of 10^{-4} Pa. The raw materials were heated to 1373 K in 10 h, soaked at this temperature for 20 h and quenched in water, further annealed at 950 K for 72 h and furnace cooled to room temperature. The obtained ingots were ground into fine powder in an agate mortar, then filled into a graphite mold with diameter of 15 mm and sintered by an SPS system (Sinter Land INC, Japan) at 773 K under axial pressure of 50 MPa for 5 minutes. The obtained pellets were cut into 3 × 3 × 12 mm^3 cuboids for electrical transport measurements and 6 × 6 × 2 mm^3 cuboids for thermal expansion coefficient measurements.

2. Thermoelectric Properties Characterizations

The Seebeck coefficient and electrical conductivity were measured using a commercial system (ADVANCE RIKO ZEM-3, Japan) in a dilute argon atmosphere, the measurement uncertainty is about 5% for both parameters. Thermal conductivity (κ_{tot}) was determined using the equation $\kappa_{tot} = D\rho C_p$, where D is the thermal diffusion coefficient, ρ is the mass density, and C_p is the specific heat capacity. The thermal diffusion coefficient (D) was measured by the laser pulse method (NETZSCH LFA467, Germany) in a nitrogen environment. The uncertainty of thermal conductivity is about 7%. The electronic thermal conductivity (κ_{ele}) is calculated according to Wiedemann-Franz law: $\kappa_{ele} = \sigma LT$, where the Lorenz factor (L) can be roughly estimated by the equation: $L = 1.5 + \exp(-|S|/116)$. Considering the uncertainties of all the parameters, the uncertainty of the calculated ZT is about 13%. The sample density was calculated using the Archimedes method, while the specific heat capacity was approximated by the Dulong-Petit limit. Carrier concentration and mobility at room temperature were obtained using the Van der Pauw method with a commercial setup (Lake Shore 8400 Series, USA), with an uncertainty of about 10%.

3. Phase and Microstructure Characterizations

Powder X-ray diffraction (XRD) patterns were collected from finely ground samples using an X-ray diffractometer (Rigaku, Japan, Cu-Kα radiation) operating at 40 kV and 20 mA. The 2θ scanning range was set from 20° to 80° with a scan rate of 8°/min. Microstructure and elemental distribution at the micron-scale were examined using a scanning electron microscope (SEM, Hitachi SU8020, Japan) equipped with energy-dispersive X-ray spectroscopy (EDS).

Samples for (scanning) transmission electron microscopy investigations were prepared using focused ion beam milling in an FEI Helios NanoLab 460F1 dual beam system. A final thickness of about 50 – 100 nm was achieved. Further thinning often causes lamellar breaking and/or severe structural degradation, thus an ultrathin specimen is hardly prepared. Selected area electron diffraction was performed on ground particles dispersed on holy carbon grid in an FEI Tecnai F20 transmission electron microscope running at 200 kV. Spherical aberration corrected high-angle annular dark-field (HAADF) scanning transmission electron microscopy (STEM) images and atomic-resolution EDS mapping were recorded using a Thermo Fisher Scientific Spectra 30-300 microscope equipped with a high brightness field emission gun, a Super-X energy dispersive X-ray detector. The acceleration voltage is 300 kV. The convergence and

collection semi-angles are 25 and 77 – 200 mrad, respectively. Image simulation was performed in Dr. Probe for experimental conditions.[1]

4. Mechanical Properties

To investigate the room temperature mechanical properties, the Vickers microhardness was measured by applying a force of 0.5 kg for 10 s (HV-1000, Shanghai BINGYU, China), and each data was the average value of 5 individual tests.

5. Density Functional Theory Calculations

Density functional theory calculations were performed using the projector augmented wave (PAW) method,[2] as implemented in the Vienna Ab initio Simulation Package (VASP),[3] with the Perdew, Burke, and Ernzerhof (PBE) generalized gradient approximation (GGA) utilized for the exchange-correlation energy functional. The DFT+U method was used to describe transition metal Mn with localized d electrons, and the effective interaction parameter $U_{eff} = U - J$ values were 5 eV. A 2 × 3 × 1 supercell of $GeMnTe_2$ (48 atoms) is adopted.[4] The pristine $Ge_{12}Mn_{12}Te_{24}$ and Sb doped cell ($Ge_{10}Mn_{10}Sb_4Te_{24}$) are fully relaxed individually with A 2 × 1 × 4 Monkhorst-Pack k-point mesh and a plane-wave cutoff energy of 500 eV until the forces on atoms were smaller than 1×10^{-3} eV/Å.[5] The energy convergence criterion of 10^{-6} eV were employed for all calculations. In the calculation of density of state (DOS), a denser k-point mesh (4 × 2 × 8) is adopted. And the special quasi-random structure (SQS) approach implemented in the "mcsqs" code of the Alloy Theoretic Automated Toolkit (ATAT) was used to create the supercell, because it can mimic a disordered structure within a small unit cell by reproducing the most relevant pair and multisite correlation functions of a random system.[6, 7] The SQS model is created based on the rock-salt structure ($Fm\bar{3}m$) in a 48-atom supercell ($Ge_{12}Mn_{12}Te_{24}$, $Ge_{10}Mn_{10}Sb_4Te_{24}$, where Ge, Mn, and Sb are located at cationic sites, Te occupies the anionic site).

For the calculations of vacancy formation energy, we used the following formula:

$$E_{\mathrm{f}} = E(\mathrm{defect}) - E(\mathrm{pure}) - \sum_{\mathrm{i}} n_{\mathrm{i}}\mu_{\mathrm{i}} \qquad \text{(S1)}$$

E(defect) and *E(pure)* are the total energies of unit cells with and without defect separately. $n_i\mu_i$ is the reference energy of n_i added atoms of element i with chemical potential μ_i.

6. Weighted Mobility

The temperature-dependent weighted mobility (μ_w) was derived from the experimental electrical conductivity σ and Seebeck coefficient S proposed by G. J. Snyder et al:[8]

$$\mu_{\mathrm{w}} = 331\frac{\mathrm{cm}^2}{\mathrm{Vs}}\left(\frac{\mathrm{m\Omega\cdot cm}}{\rho}\right)\left(\frac{T}{300\,\mathrm{K}}\right)^{-3/2}\left[\frac{\exp\left(\frac{|S|}{k_{\mathrm{B}}/e}-2\right)}{1+\exp\left(-5\left(\frac{|S|}{k_{\mathrm{B}}/e}-1\right)\right)}+\frac{\frac{3}{\pi^2}\frac{|S|}{k_{\mathrm{B}}/e}}{1+\exp\left(5\left(\frac{|S|}{k_{\mathrm{B}}/e}-1\right)\right)}\right] \quad \text{(S2)}$$

Here, μ_w is the weighted mobility, ρ is the electrical resistivity measured in mΩ cm, T is the absolute temperature in K, S is the Seebeck coefficient, and k_B/e = 86.3 μV K^{-1}.

7. Details of the Debye-Callaway Model

Using the Debye-Callaway model, the final temperature (T)-dependent can be expressed as a sum κ_{lat} (T) of the spectral lattice thermal conductivity from different frequencies:

$$\kappa_{\mathrm{lat}} = \int \kappa_s(\omega)d\omega = \frac{1}{3}\int_0^{\omega_a} C_s(\omega)v_g(\omega)^2\tau_{tot}(\omega)d\omega \quad \text{(S3)}$$

Thus, the $\kappa_s(\omega)$ is determined by the $C_s(\omega)$, the frequency-dependent phonon group velocity $v_g(\omega)$ and total relaxation time $\kappa_{tot}(\omega)$. Generally, as the phonons in optical branches shows low velocity, only the phonons in acoustic branches are considered to calculate the κ_{lat}. Thus, the cut-off frequency for acoustic branches ω_a is given by $\omega_a = \left(\frac{6\pi^2}{V_{\mathrm{cell}}}\right)^{1/3}$, $v_s = \left(\frac{6\pi^2}{NV_{\mathrm{av}}}\right)^{1/3}$, where N, V_{av} and v_s the atomic numbers in a primitive cell, average atomic volume and sound speed respectively. For simple approximation, the frequency-dependent phonon group velocity $v_g(\omega)$ is set as a constant value v_s, and κ_{lat} is calculated by the following equation:

$$\kappa_{\mathrm{lat}} = \frac{k_B}{2\pi^2 v_s}\left(\frac{k_B}{h}\right)\int_0^{\theta_D/T}\tau_{tot}(x)\frac{x^4e^x}{(e^x-1)^2}dx \quad \text{(S4)}$$

$$\theta_a = \hbar\omega_a/k_B = \left(\frac{6\pi^2}{NV_{\mathrm{av}}}\right)^{1/3}\hbar v_s/k_B \quad \text{(S5)}$$

The dimensionless variable x in equation is defined as $x = \hbar\omega/k_BT$, where ω is the phonon frequency. The $\tau_{tot}(x)$ is the reciprocal sum of the relaxation-times from different scattering mechanisms according to the Matthiessen's rule:

$$\tau = \tau_U^{-1} + \tau_N^{-1} + \tau_B^{-1} + \tau_{PD}^{-1} + \tau_{vdW}^{-1} \quad \text{(S6)}$$

Where τ_U^{-1}, τ_N^{-1}, τ_B^{-1}, τ_{PD}^{-1} and τ_{vdW}^{-1} are the contributions from the Umklapp phonon-phonon scattering, normal phonon-phonon scattering, boundary scattering, point-defect scattering and localized van der Waals gaps scattering.

The τ_U^{-1} is calculated from the following equation:

$$\tau_U^{-1} = \frac{2k_B^3 V_{av}^{1/3} \gamma^2 T^3}{(6\pi^2)^{1/3} M_{av} v_s \hbar^2} x^2 \exp(-\frac{\theta_a}{bT}) \quad \text{(S7)}$$

Where γ and M_{av} are the Gruneisen parameter, and the atomic mass, respectively.

The τ_N^{-1} is calculated from the following equation:

$$\tau_N^{-1} = B_N \tau_U^{-1} \quad \text{(S8)}$$

Where B_N is the ratio of normal phonon scattering to Umklapp scattering.

The τ_B^{-1} is calculated from the following equation:

$$\tau_B^{-1} = \frac{v_s}{D} \quad \text{(S9)}$$

Where v_s is the average sound velocity and D is the experimentally determined grain size.

The τ_{PD}^{-1} is calculated from the following equation:

$$\tau_{PD}^{-1} = \frac{V_{av}\Gamma}{4\pi v_s^3} \omega^4 = \frac{V_{av}\Gamma}{4\pi v_s^3} (\frac{k_B T}{h})^4 x^4 \quad \text{(S10)}$$

Where Γ is the disorder scattering parameter.

The τ_{vdW}^{-1} is calculated from the following equation:

$$\tau_{vdW}^{-1} = 0.7 \frac{a_{lat}^2 \gamma^2 N_s}{v_s^2 \omega^2} \quad \text{(S11)}$$

Where a_{lat}, γ, N_s, v_s and ω are the average lattice parameter, Grüneisen parameter, density of gaps, sound speed and frequency, respectively.

Detailed parameters are shown in **Table S1**.[9-11]

Table S1. Parameters of Debye-Callaway model

Parameter	Symbol	Values	Source
Average atomic mass/kg	M_{av}	$1.764*10^{-25}$	experiments
Average atomic mass volume/kg	V_{av}	$2.554*10^{-29}$	experiments
Grüneisen parameter	γ	1.4833	Ref.11
Average sound velocity (m/s)	v_s	2362	Ref.9
Longitudinal velocity (m/s)	v_L	3670	Ref.9
Transverse velocity (m/s)	v_T	2129	Ref.9
Debye temperature (K)	Θ_a	239	experiments
Umklapp to normal ratio	B_N	3.5	fitted
Characteristic of the vibrational	b	0.9	fitted
Grain size (m)	D	$3*10^{-5}$	experiments
Disorder scattering parameter	Γ	0.1	fitted
Density of gaps (m^{-2})	N_s	$3.25*10^{7}$	fitted
Lattice constant	a_{lat}	$5.89*10^{-10}$	experiments

Supporting Figures:

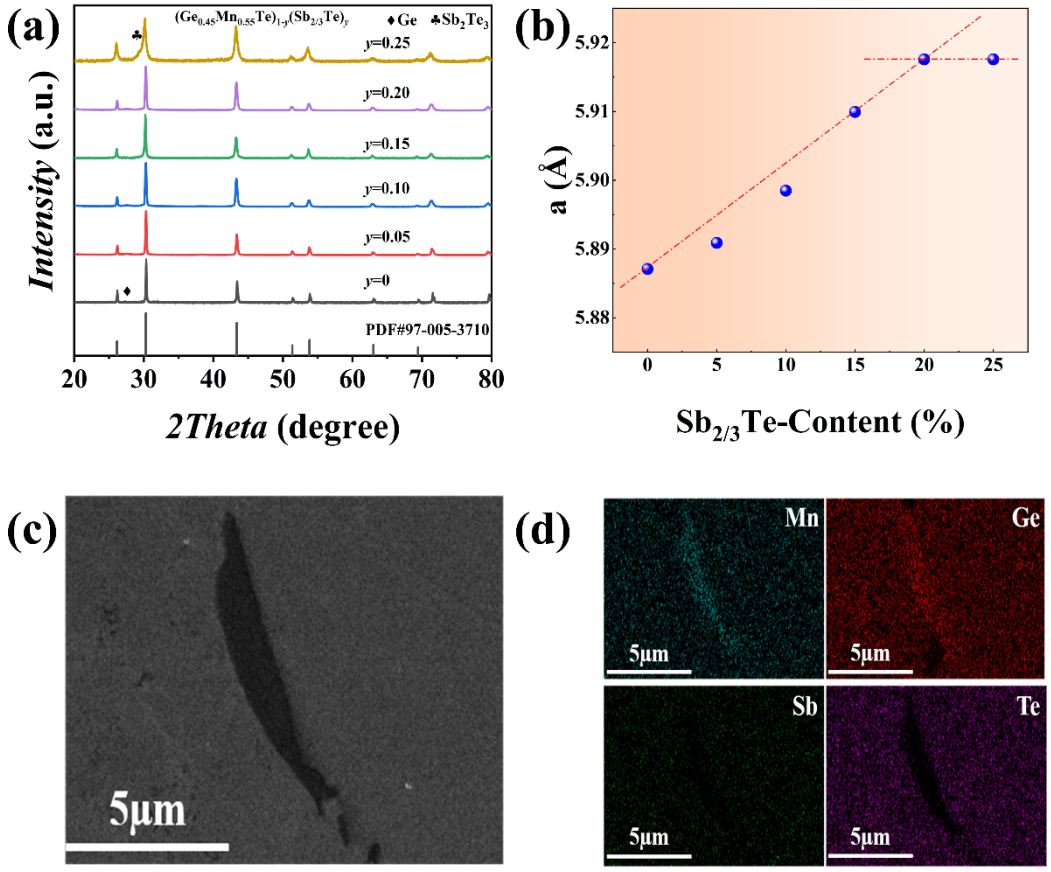

Figure S1. (a) Room temperature powder XRD diffraction pattern of $(Ge_{0.45}Mn_{0.55}Te)_{1-y}(Sb_{2/3}Te)_y$ (y = 0.05, 0.1, 0.15, 0.2 and 0.25), (b) measured lattice constants, (c) micron-scale precipitate and (d) EDS patterns in the sample with y = 0.05.

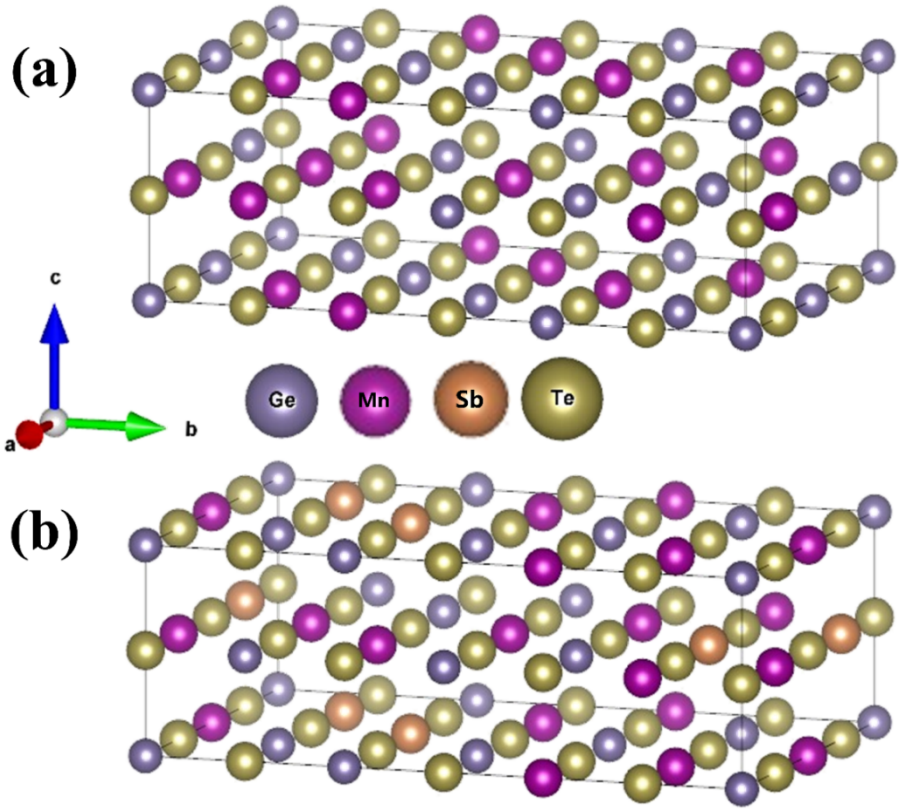

Figure S2. Detailed special quasi-random structure of (a) $Ge_{12}Mn_{12}Te_{24}$ and (b) $Ge_{10}Mn_{10}Sb_4Te_{24}$ used for DFT calculations.

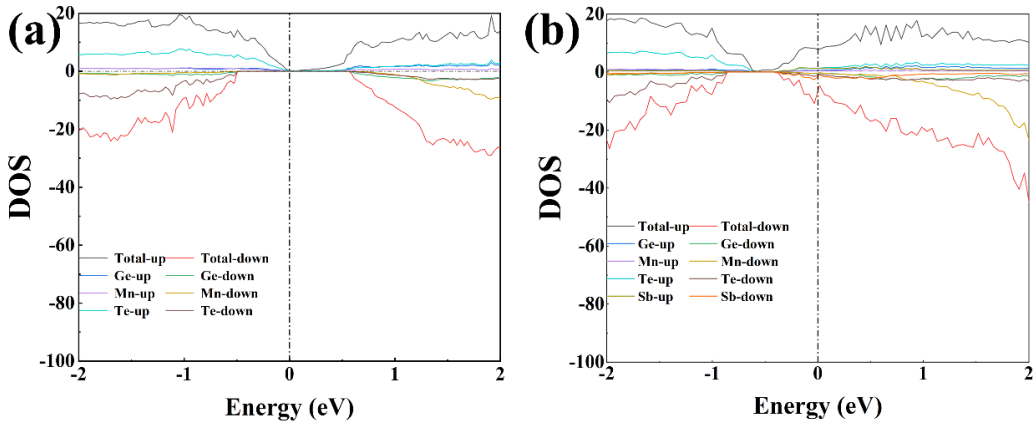

Figure S3. Density of state (DOS) and Partial density of state (PDOS) for (a) $Ge_{12}Mn_{12}Te_{24}$ and (b) $Ge_{10}Mn_{10}Sb_4Te_{24}$.

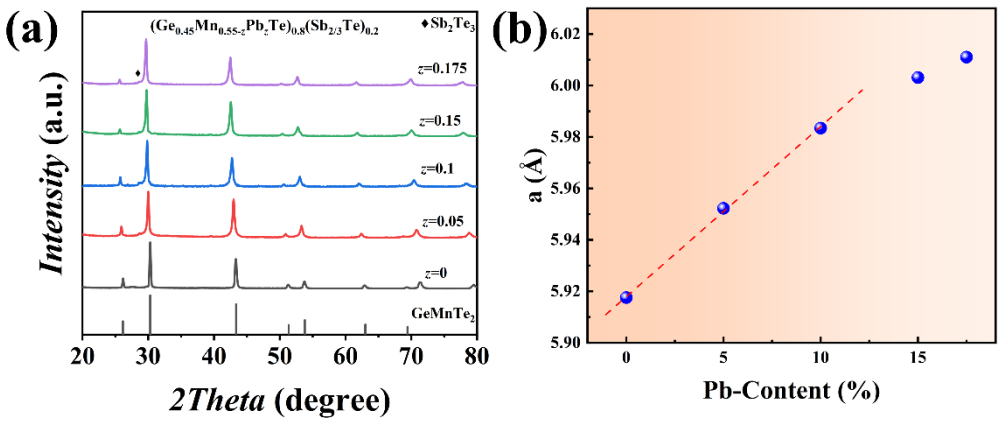

Figure S4. (a) Room-temperature powder XRD diffraction pattern of $(Ge_{0.45}Mn_{0.55-z}Pb_zTe)_{0.8}(Sb_{2/3}Te)_{0.2}$ (z = 0, 0.05, 0.1, 0.15 and 0.175), and (b) calculated lattice constants.

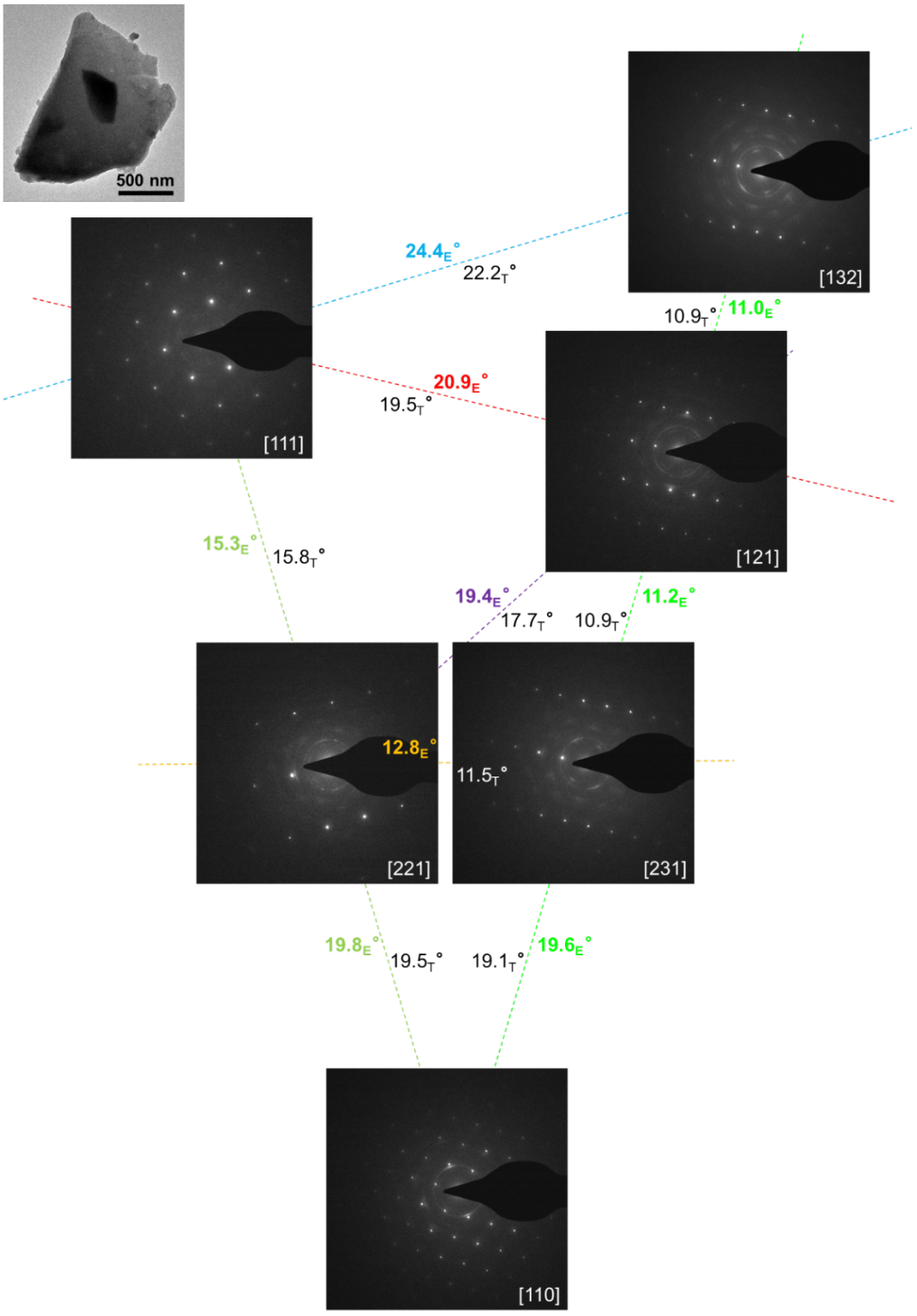

Figure S5. Systematic tilting series of selected area electron diffraction revealing the cubic phase structure of $(Ge_{0.45}Mn_{0.4}Pb_{0.15}Te)_{0.8}(Sb_{2/3}Te)_{0.2}$. Values with subscripts E and T denote the experimentally measured and theoretically calculated angles between the adjacent directions.

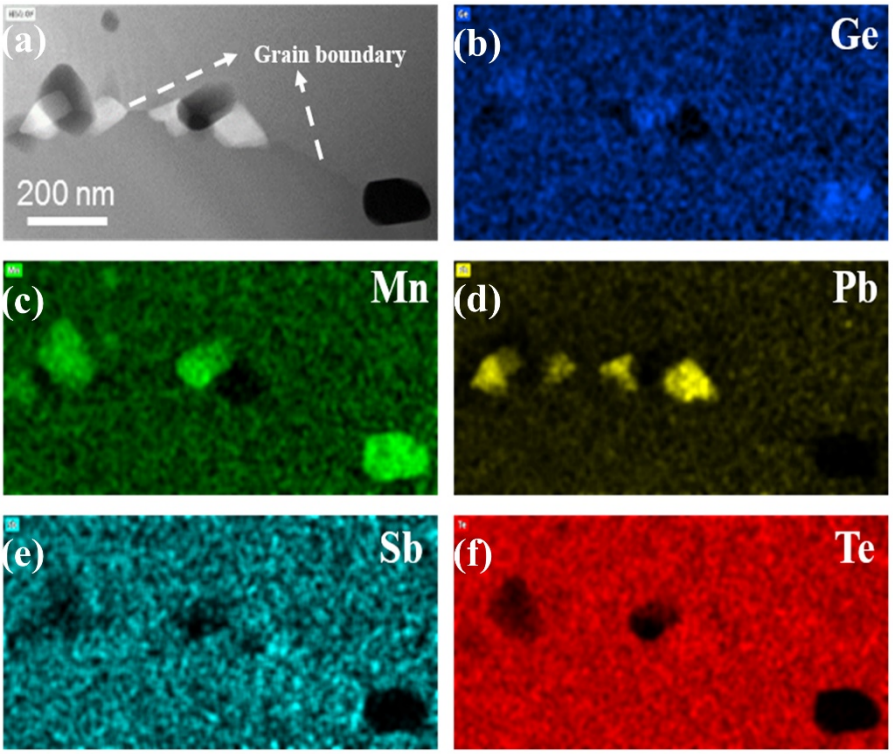

Figure S6. (a) Low-magnification HAADF STEM image and (b)-(f) corresponding EDS maps showing PbTe and Ge/Mn-rich precipitates in the $(Ge_{0.45}Mn_{0.4}Pb_{0.15}Te)_{0.8}(Sb_{2/3}Te)_{0.2}$ sample.

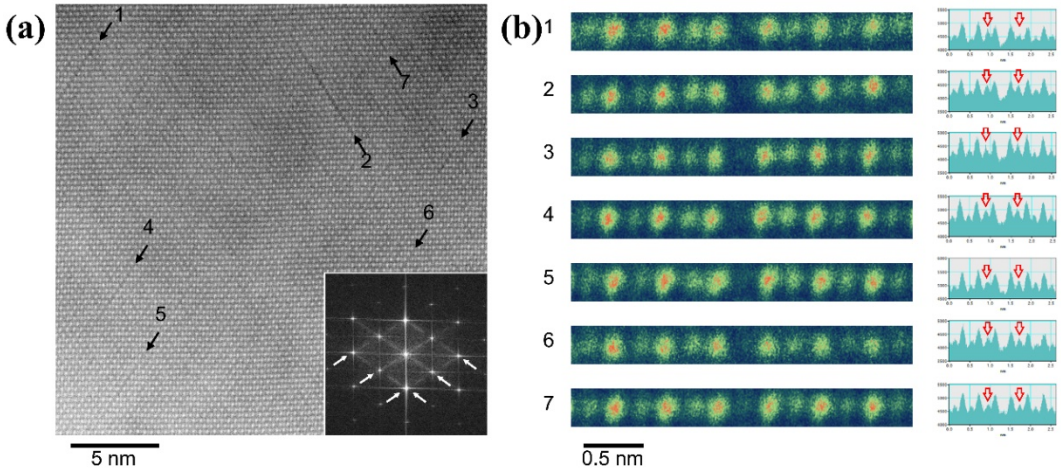

Figure S7. (a) HAADF STEM image and corresponding FFT (inset) showing the presence of localized vdW gaps in $(Ge_{0.45}Mn_{0.4}Pb_{0.15}Te)_{0.8}(Sb_{2/3}Te)_{0.2}$. (b) Layer-by-layer averaged images of localized vdW gaps indicated by 1 – 7 in (a) and corresponding intensity line profiles of the atomic columns across the vdW gaps. Red arrows mark cation columns with higher intensity.

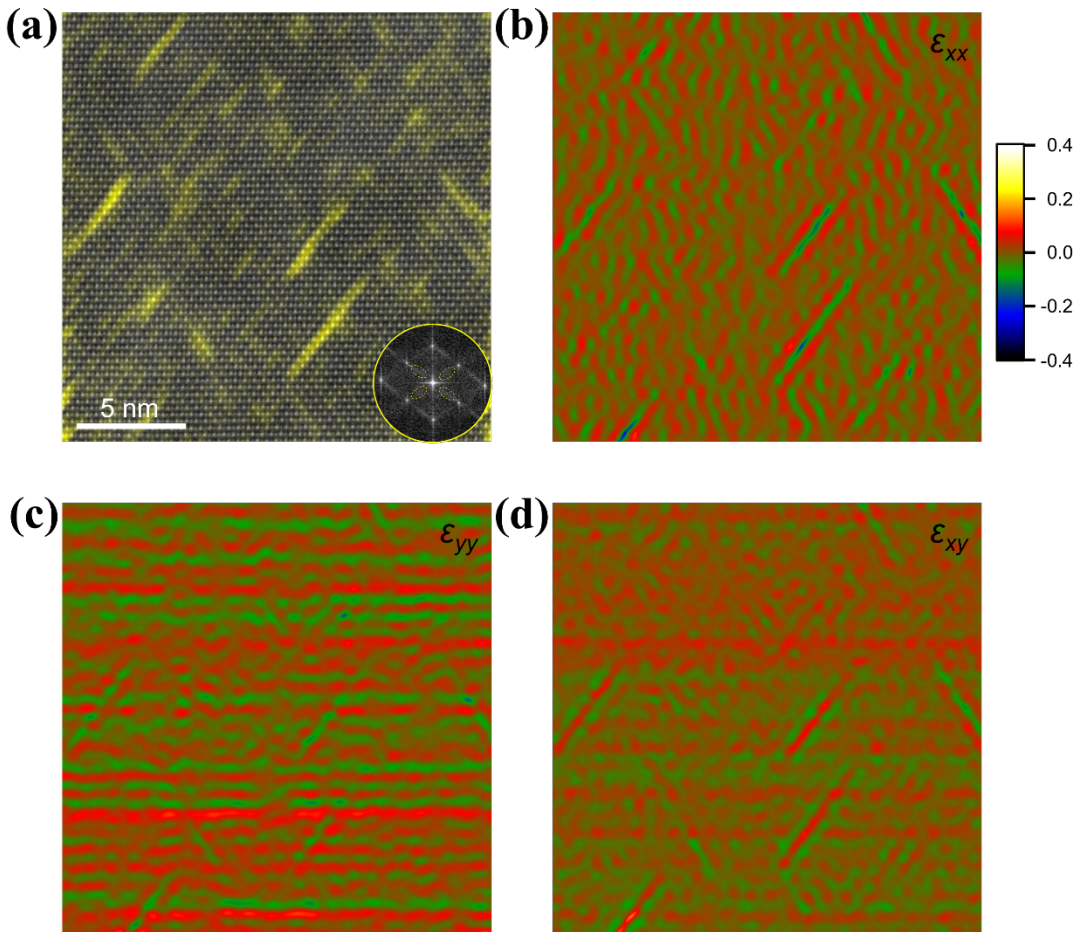

Figure S8. (a) Digital dark-field image (*i.e.*, inverse Fourier transform) generated by using the selected streak areas (see dashed ellipses) highlights the localized vdW gaps. (b) to (d) Strain components of ε_{xx}, ε_{yy} and ε_{xy}, respectively, calculated by using geometric phase analysis.[12]

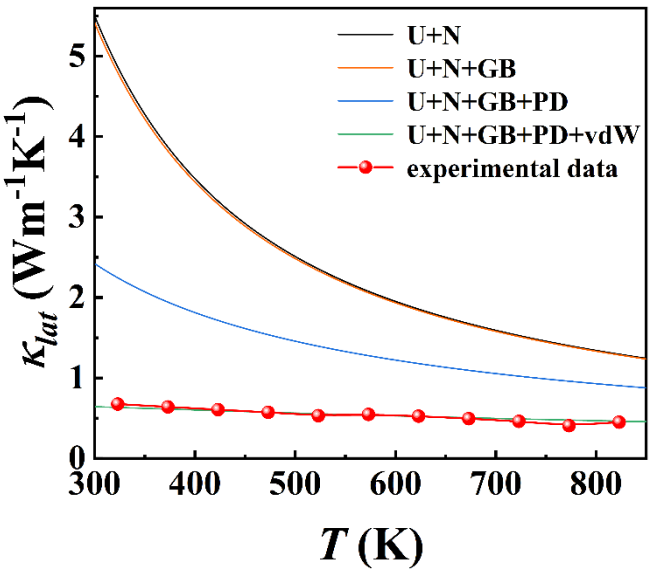

Figure S9. Fitting of temperature-dependent lattice thermal conductivity κ_{lat} of the $(Ge_{0.45}Mn_{0.4}Pb_{0.15}Te)_{0.8}(Sb_{2/3}Te)_{0.2}$ sample using Debye-Callaway model by considering Umklapp phonon-phonon scattering (U), normal phonon-phonon scattering (N), boundary scattering (B), point defect scattering (PD) and van der Waals gaps scattering (vdW) processes.

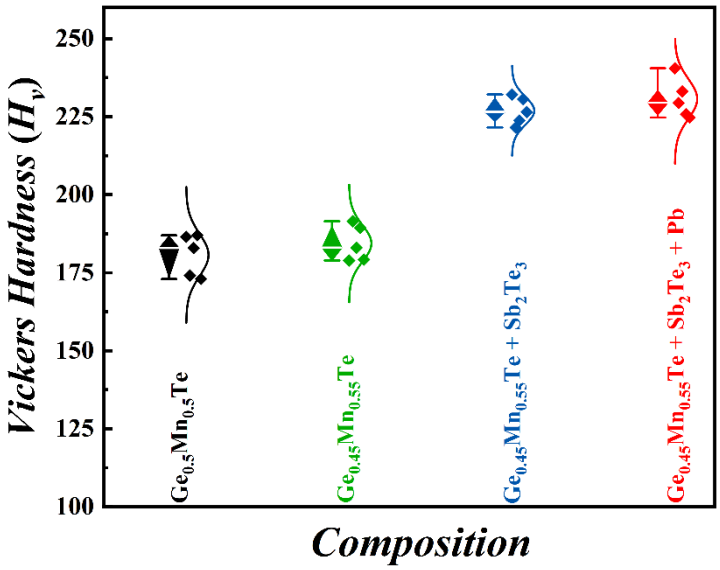

Figure S10. Stepwise enhancements of Vickers hardness (H_v) in this work.

References

[1] J. Barthel, "Dr. Probe: A software for high-resolution STEM image simulation," *Ultramicroscopy* **2018**, *193*, 1-11. https://doi.org/10.1016/j.ultramic.2018.06.003.

[2] P. E. Blöchl, "Projector augmented-wave method," *Phys. Rev. B* **1994**, *50*, 17953-17979. https://doi.org/10.1103/PhysRevB.50.17953.

[3] V. Wang, N. Xu, J.-C. Liu, G. Tang, W.-T. Geng, "VASPKIT: A user-friendly interface facilitating high-throughput computing and analysis using VASP code," *Comput. Phys. Commun.* **2021**, *267*, 108033. https://doi.org/10.1016/j.cpc.2021.108033.

[4] M. Zou, H. Dong, Y. Lu, T. Wang, D. Su, Y. Wang, X. Pan, Y. Zou, "Determining the formation enthalpies and phase diagram of high-density uranium fuels by mixing GGA and GGA + U calculations," *Comput. Mater. Sci.* **2025**, *249*, 113626. https://doi.org/10.1016/j.commatsci.2024.113626.

[5] H. J. Monkhorst, J. D. Pack, "Special points for Brillouin-zone integrations," *Phys. Rev. B* **1976**, *13*, 5188-5192. https://doi.org/10.1103/PhysRevB.13.5188.

[6] G. Lakits, A. Arnau, H. Winter, "Slow-particle-induced kinetic electron emission from a clean metal surface: A comparison for neutral and ionized projectiles," *Phys. Rev. B* **1990**, *42*, 15-24. https://doi.org/10.1103/PhysRevB.42.15.

[7] A. van de Walle, P. Tiwary, M. de Jong, D. L. Olmsted, M. Asta, A. Dick, D. Shin, Y. Wang, L.-Q. Chen, Z.-K. Liu, "Efficient stochastic generation of special quasirandom structures," *Calphad* **2013**, *42*, 13-18. https://doi.org/10.1016/j.calphad.2013.06.006.

[8] G. J. Snyder, A. H. Snyder, M. Wood, R. Gurunathan, B. H. Snyder, C. Niu, "Weighted Mobility," *Adv. Mater.* **2020**, *32*, 2001537. https://doi.org/10.1002/adma.202001537.

[9] Q. Mei, C. Xie, J. Liu, Y. Wang, J. Cui, L. Liao, C. Liao, W. Xu, S. Li, Q. Zhang, X. Tang, G. Tan, "Unveiling the Role of Nontrivial Electronic Structure and Lattice Softening in the Excellent Thermoelectric Performance of $MnGeTe_2$ Alloys near the Ioffe–Regel Limit," *Adv. Energy Mater.* **2025**, *15*, 2500937. https://doi.org/10.1002/aenm.202500937.

[10] M. Caro, A. Tamm, A. A. Correa, A. Caro, "Role of electrons in collision cascades in solids. I. Dissipative model," *Phys. Rev. B* **2019**, *99*, 174301. https://doi.org/10.1103/PhysRevB.99.174301.

[11] J. Dong, Y. Jiang, Y. Sun, J. Liu, J. Pei, W. Li, X. Y. Tan, L. Hu, N. Jia, B. Xu, Q. Li, J.-F. Li, Q. Yan, M. G. Kanatzidis, "Discordant Distortion in Cubic $GeMnTe_2$ and High Thermoelectric Properties of $GeMnTe_2$-*x*%SbTe. *J. Am. Chem. Soc.* **2023**, *145*, 1988-1996. https://doi.org/10.1021/jacs.2c12877.

[12] M. J. Hÿtch, E. Snoeck, R. Kilaas, "Quantitative measurement of displacement and strain

fields from HREM micrographs," *Ultramicroscopy* **1998**, *74*, 131-146. https://doi.org/10.1016/S0304-3991(98)00035-7.